ENCIT 2018

ABCM Associação Brasileira de Engenharia e Ciências Mecânicas

17th Brazilian Congress of Thermal Sciences and Engineering
November 25th-28th, 2018, Águas de Lindóia, SP, Brazil

ENCIT2018-0761
EFFECT OF BLOOD RHEOLOGY MODEL ON HEMODYNAMIC PARAMETERS RELATED TO INTRACRANIAL ANEURYSM RUPTURE

Iago Lessa de Oliveira
Gabriel Bertacco dos Santos
José Luiz Gasche
São Paulo State University (UNESP), School of Natural Sciences and Engineering, Ilha Solteira, São Paulo, Brazil
iago.oliveira@unesp.br
gabriel.bertacco@unesp.br
gasche@dem.feis.unesp.br

Julio Militzer
Dalhousie University, Department of Mechanical Engineering, Halifax, Nova Scotia, Canada
julio.militzer@dal.ca

Carlos Eduardo Baccin
Interventional Neuroradiology, Hospital Israelita Albert Einstein, São Paulo, Brazil
cebaccin@gmail.com

Abstract. *Aneurysms are abnormalities formed in some regions of the human vascular system and are characterized by dilated and thin regions of the arterial wall. One of the most common types occurs inside the brain arteries in the circle of Willis. These intracranial aneurysms are extremely dangerous because in case of rupture they can cause subarachnoid hemorrhage, with consequent death or presence of permanent damage to the patient. Causes of aneurysms have been investigated for a long time, and researchers agree that hemodynamic effects play a key role in the rupture of brain aneurysms. With the development of scanning techniques of the cerebral vascular system, it has been possible to obtain the geometry of aneurysms allowing numerical methods for the solution of blood flow to be used. Since then, several researchers have been investigating the influence of biological and hemodynamic variables on aneurysms rupture considering arteries and aneurysms as rigid walls. However, few studies analyze the influence of the blood rheology model on these parameters. In this work we simulated the blood flow in patient-specific aneurysm geometries using the open-source library* `foam-extend-4.0` *with different blood rheology models. By comparing the flow parameters – wall shear stress and flow velocity field – between the results of the simulations, we assess the influence of these models on the hemodynamic of flow in intracranial aneurysms.*

Keywords: ***Intracranial aneurysms. Numerical simulation. Blood rheology. Rupture***

1. INTRODUCTION

An aneurysm is an arterial disease defined as a dilated region of the artery wall, which arise at different sites of the human vascular system, more commonly found on the abdominal aorta and arteries that reach the brain. Intracranial aneurysms generally occur at arterial bifurcations of the circle of Willis – formed by the internal carotid arteries, the vertebro-basilar system and their branches – or at nearby locations and their size can vary from 1 mm to 25 mm and even larger. Figure 1a schematically shows an aneurysm with its main geometric parameters and Fig. 1b depicts the brain vessels tree.

Estimates show that 2 up to 5% of the world's population have intracranial aneurysms (Qureshi *et al.*, 2007). The main consequences of this disease occur when the aneurysm ruptures, which represent a high risk to the patient, causing a mortality rate between 40 and 50% and also present high risk of permanent injury. It is reported that 85% of Subarachnoid Hemorrhage (SAH) cases, a devastating event that can be fatal or lead to a severe neurological deficit, are caused by the rupture of these aneurysms (van Gijn *et al.*, 2001; Van Gijn *et al.*, 2007; Zacharia *et al.*, 2010). Hop *et al.* (1997) concluded that fatal cases of SAH occurred from 32 to 67% and about one-third of morbidity among the patients who survived. The work of The International Study of Unruptured Intracranial Aneurysms Investigators (2003), one of the most relevant scientific works on rupture of intracranial aneurysms being used until today for the decision of their treatment, evaluated the probability of SAH over time for a group of 1,077 patients – followed up over 4.1 years – who had no previous cases of SAH, for different aneurysm sizes and concluded that the risk of SAH increases over time and for larger aneurysms.

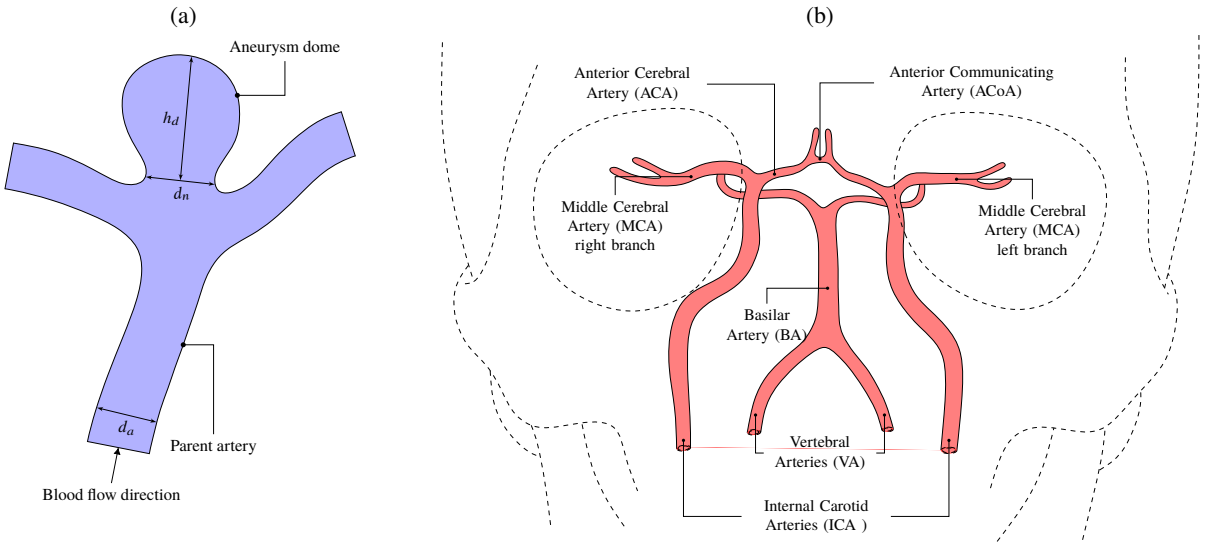

Figure 1. (a) Aneurysm dome, its parent artery, aneurysm dome height, h_d, and d_n, the neck diameter, definitions; the parent artery has diameter d_a; (b) Frontal view of the skull with the location of the main arteries of the brain arteries tree, with the most common bifurcations where aneurysms can grow.

The same study reported that 27% patients died of intracranial hemorrhage of 193 patients who died during the follow up period.

With the development of computational imaging techniques – such as three-dimensional (3D) Digital Subtraction Angiography (DSA), 3D Rotational Angiography, Magnetic Resonance Angiography and Computed Tomography Angiography (Cebral *et al.*, 2003; Wong *et al.*, 2011) –, the geometry of patient-specific intracranial aneurysms can be obtained, allowing numerical simulations of the flow in realistic blood vessels and aneurysms through Computational Fluid Dynamics (CFD) (Steinman *et al.*, 2003; Shojima *et al.*, 2004; Torii *et al.*, 2008; Bazilevs *et al.*, 2010; Lu *et al.*, 2011; Fukazawa *et al.*, 2015). These studies, together with medical studies, helped elucidate biological aspects of the aneurysm disease and showed that hemodynamic effects are probably responsible for intracranial aneurysms formation, evolution and rupture. However, most numerical studies so far have used simplified hypothesis for the aneurysm flow modeling, such as considering blood as a Newtonian fluid (Bazilevs *et al.*, 2010; Isaksen *et al.*, 2008; Torii *et al.*, 2007; Lee *et al.*, 2013), although knowing that blood behaves as a non-Newtonian fluid. Specific works comparing simulations results with different rheology models exist in the literature, but mainly for flow in arteries (Perktold *et al.*, 1991) and few for patient-specific aneurysms geometries (Bernsdorf and Wang, 2009). This is an important point to consider because aneurysms can reach large dimensions compared to their surrounding arteries and, as it is well agreed in the literature, blood's apparent viscosity is shear strain dependent (Fung, 1993). Therefore, due to the size and shape variability of intracranial aneurysms, it could be important to take into account the non-Newtonian behavior of blood when simulating flow in certain types of aneurysms.

Hence, the aim of this work is to analyze what is the effect of different blood rheology models on the hemodynamic parameters that are related to aneurysm rupture, such as velocity field and Wall Shear Stress (WSS). We intend to do this by simulating different patient-specific aneurysms cases regarding size, shape and location in the brain vessels tree.

2. METHODOLOGY

2.1 Physical and Mathematical Modeling

We consider blood as a homogeneous incompressible fluid in an isotherm laminar flow regime – the velocities found in an aneurysm flow yield a Reynolds number based on the Newtonian fluid model, Re, of about 600 to 700, based on the parent artery diameter and on the dynamic viscosity of blood as a Newtonian fluid equal to 3.5×10^{-3} Pa s (Shibeshi and Collins, 2005; Isaksen *et al.*, 2008). The blood density was considered to be 1,056 kg/m^3 (Isaksen *et al.*, 2008; Robertson *et al.*, 2009). We present in Section 2.2 the rheological models used for blood. The aneurysm and arteries walls were considered to be rigid. This is a strong hypothesis, however it has been used extensively to study blood flow by numerical techniques when accounting for its non-Newtonian behavior.

The equations governing the flow are the continuity equation for incompressible flows, derived from mass conservation

principle, written in integral form for a fixed control volume V, with surface S, as:

$$\oint_S \rho^{\mathrm{f}} \boldsymbol{v} \cdot \boldsymbol{n} \mathrm{d}S = 0 \tag{1}$$

where $\boldsymbol{n}$ is the unit normal vector to S pointing outwards and $\boldsymbol{v}$ is the flow velocity field; the momentum equation, derived from the balance of linear momentum in integral conservative form:

$$\frac{\partial}{\partial t} \int_{V(t)} \rho^{\mathrm{f}} \boldsymbol{v}\left(\boldsymbol{x}, t\right) \mathrm{d}V + \oint_{S(t)} \rho^{\mathrm{f}} \boldsymbol{v}\boldsymbol{v} \cdot \boldsymbol{n} \mathrm{d}S = -\oint_{S(t)} p\boldsymbol{n} \mathrm{d}S + \oint_{S(t)} \boldsymbol{\tau} \cdot \boldsymbol{n} \mathrm{d}S \tag{2}$$

where p is the pressure field and $\boldsymbol{\tau}$ is the viscous part of the Cauchy stress tensor, which depends on the rheological model. We employed different viscosity models, which are discussed in Section 2.2

Boundary and Initial Conditions

To close the mathematical problem composed of Eqs. (1) and (2), we further need to specify the initial and boundary conditions. For the initial condition, we used an already available velocity and pressure fields generated by solving the same problem in coarser meshes (as part of the mesh-convergence tests). The boundary conditions were:

- Inlet: the inlet is a cross section located in the parent artery of the aneurysm – see Fig. 1a where the blood flow entrance is indicated – which depends on the aneurysm branch location. The condition imposed is a specified time-varying flow rate, corresponding to the flow pulse from the beginning of systole until the end of the diastole. Such waveform profile, measured in the internal carotid by Ford *et al.* (2005), is shown in Fig. 2a as a normalized flow rate based on the temporal average blood flow rate. Since the aneurysms studied here are located in different bifurcations of the brain vessels tree, we calculated the inlet flow rate multiplying this normalized flow rate by the average blood flow rate of the artery of interest. The average blood flow rate, $\bar{q}_a$, for different portions of the brain vessels tree was provided by Zarrinkoob *et al.* (2015), who measured it as a percentage of the total blood flow rate to the brain vessels for normal subjects (11.95 ± 2.05) ml/s, as shown in Fig. 2b, which presents the mean and the standard deviation values. At the inlet, the pressure gradient was set to zero.

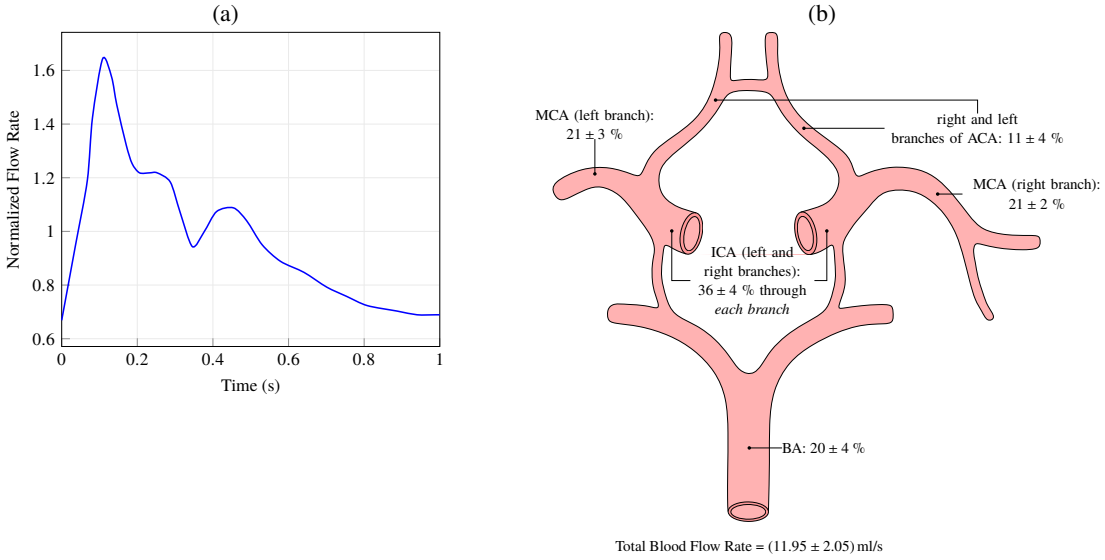

Figure 2. (a) Experimental normalized flow rate for the internal carotid (prepared by the authors with data provided by Ford *et al.* (2005)); (b) Average blood flow rate through the arteries of the brain as a percentage of the total blood flow rate entering the brain, with each respective standard deviation (prepared by the authors with data from Zarrinkoob *et al.* (2015)).

- Outlets: the outlets are located on the vessels after the aneurysm bifurcation. We used a constant pressure at the outlets, corresponding to the averaged human body pressure level for a cardiac cycle, i.e. ≈ 100 mmHg (13,333 Pa), to directly obtain the correct pressure levels on the results;
- Wall: the wall was considered rigid, therefore a Dirichlet boundary conditions is imposed for the velocity filed, associated with zero mass flux and a zero pressure gradient.

2.2 Rheological Models for Blood

We employed different models for blood rheology: the Newtonian fluid model and typical non-Newtonian models which capture the phenomena exhibited by blood departing from the Newtonian behavior, such as shear-thinning and yield stress (Cokelet *et al.*, 1963; Robertson *et al.*, 2009; Sochi, 2013). The literature reports several models that have already been used to simulate blood behavior, but the most used ones are known as Casson and Carreau-Yasuda models (Fung, 1993; Shibeshi and Collins, 2005; Robertson *et al.*, 2009). For the Newtonian incompressible fluid model, the full tensorial constitutive equation for three-dimensional flows is:

$$\boldsymbol{\tau} = \mu^{\mathrm{f}} \left(\nabla \boldsymbol{v} + \nabla^{\mathrm{T}} \boldsymbol{v} \right) \tag{3}$$

where μ^{f} is the dynamic viscosity of blood, which we considered to be 3.5×10^{-3} Pa s (Shibeshi and Collins, 2005; Isaksen *et al.*, 2008). Equation (3) can be directly substituted into Eq. (2) to yield, together with Eq. (1), the Navier-Stokes equations.

The constitutive equations for the non-Newtonian models chosen are generally provided by the literature for simple shear flows – or other *rheometric flows* –, hence they provide only the shear components of the stress and shear tensors. For Casson's model, we have:

$$\sqrt{\tau} = \sqrt{\tau_C} + \sqrt{k}\sqrt{\dot{\gamma}} \tag{4}$$

where τ_C is interpreted as the yield stress and k is a constant (Fung, 1993). This model captures both shear-thinning and yield stress characteristics of blood behavior. This behavior when the shear rate tends to zero is very debated in the literature (Cokelet *et al.*, 1963; Fung, 1993), but the problems in determining this behavior is intrinsic of the type of measurement itself, i.e. the difficulty in performing measurements when $\dot{\gamma} \to 0$. However, in general the literature agrees that blood have a yield stress which also varies with temperature and the hematocrit level of the blood sample. From the reference ranges of hematocrit in the human blood – 36 % to 46 % in women and 41 % to 51 % in men – we used a value of 45 % for the hematocrit level to determine the blood parameters, which yields $\tau_C \approx 2.7 \times 10^{-3}$ Pa (Merrill *et al.*, 1963). The constant k was considered equal to 3.4×10^{-3} Pa s (Robertson *et al.*, 2009).

The Carreau-Yasuda model – often referred as only Carreau model – have a constitutive relation given by:

$$\frac{\eta^{\mathrm{f}}(\dot{\gamma}) - \eta^{\mathrm{f}}_{\infty}}{\eta^{\mathrm{f}}_{0} - \eta^{\mathrm{f}}_{\infty}} = \left[1 + (\lambda\dot{\gamma})^{a}\right]^{(n-1)/a}$$

which shows the shear-thinning behavior of blood with also the information of the known Newtonian-like behavior for high shear rate, with $\eta^{\mathrm{f}}_{\infty}$ being the blood viscosity on this case, and η^{f}_{0} the viscosity when $\dot{\gamma} \to 0$; we used $\eta^{\mathrm{f}}_{\infty} = 3.45 \times 10^{-3}$ Pa s, $\eta^{\mathrm{f}}_{0} = 5.6 \times 10^{-2}$ Pa s, $\lambda = 1.902$, $a = 1.25$ and $n = 0.22$, which were calibrated for human blood (Robertson *et al.*, 2009).

2.3 Tensorial Constitutive Equations for Non-Newtonian Models

As highlighted in Section 2.2 the constitutive equations for the non-Newtonian models used were defined for simple shear flows due to its empirical nature, originated from traditional rheometric measurements. A complex task would be to evaluate the complete tensorial constitutive equation for these models, which is needed to solve the governing equations presented in Section 2.1 where the viscous part of the Cauchy stress tensor is needed, $\boldsymbol{\tau}$. Since this must be a formidable task to accomplish via experimental techniques, we present here a common mathematical form to perform it (Fung, 1993).

One of the basic information provided by rheometric experiments with non-Newtonian fluids is that their viscosity depends on the shear rate, i.e. in general $\eta^{\mathrm{f}} = \eta^{\mathrm{f}}(\dot{\gamma})$. In a generic three-dimensional flow with velocity field $\boldsymbol{v}$, the shear rate is substituted by the rate-of-deformation second-order tensor, $\boldsymbol{D}$, given by:

$$\boldsymbol{D} = \frac{1}{2} \left(\nabla \boldsymbol{v} + \nabla^{\mathrm{T}} \boldsymbol{v} \right) \tag{5}$$

and in this case the apparent viscosity would be a function of the components of $\boldsymbol{D}$. Since a main hypothesis considered is that blood is an isotropic fluid, it can be proved that the scalar η^{f} is a function only of the principal invariants of the tensor $\boldsymbol{D}$, given by:

$$I_1 = \mathrm{tr}\,\boldsymbol{D} = D_{ii} \tag{6}$$

$$I_2 = \frac{1}{2}\left[(\mathrm{tr}\,\boldsymbol{D})^2 - \mathrm{tr}\,(\boldsymbol{D}\cdot\boldsymbol{D})\right] = \frac{1}{2}\left[(D_{kk})^2 - D_{ij}D_{ji}\right] \tag{7}$$

$$I_3 = \det \boldsymbol{D} = \varepsilon_{ijk} D_{i1} D_{j2} D_{k3} \tag{8}$$

For the incompressible case $I_1 = 0$ and, consequently, I_2 assumes a negative value. Therefore, to use a positive invariant value, what is usually perform is to consider the apparent viscosity as a function of a new invariant J_2, defined as:

$$J_2 \equiv \frac{1}{2} I_1^2 - I_2 = \frac{1}{2} D_{ij} D_{ij} \tag{9}$$

This procedure usually considers that there is no dependency of η^{f} on I_3 because the rheometric flows used in this type of experiment have $I_3 = 0$ (Fung, 1993). Therefore, $\eta^{\mathrm{f}} = \eta^{\mathrm{f}}(J_2)$.

To fully characterize the tensorial behavior of blood, we use the *generalized Newtonian model*, where the viscous part of the Cauchy stress tensor is given by:

$$\boldsymbol{\tau} = 2\eta^{\mathrm{f}}(J_2)\,\boldsymbol{D} \tag{10}$$

where the apparent viscosity function must be specified for each non-Newtonian model based on the constitutive relation for the one-dimensional case. For example, using the definition of apparent viscosity:

$$\eta^{\mathrm{f}} \equiv \frac{\tau}{\dot{\gamma}} \tag{11}$$

together with Casson's model constitutive equation, Eq. (4), we can show that:

$$\eta^{\mathrm{f}} = \left(\sqrt{\frac{\tau_C}{\dot{\gamma}}} + \sqrt{k} \right)^2 \tag{12}$$

and where the shear rate is defined as follows:

$$\dot{\gamma} \equiv 2\sqrt{J_2} \tag{13}$$

Finally, we can derive a final momentum balance equation for a 3D flow of a non-Newtonian fluid, by substituting Eq. (10) in Eq. (2), and using the definition of $\boldsymbol{D}$, Eq. (5). After some rearrangement we find:

$$\frac{\partial}{\partial t} \int_{V(t)} \rho^{\mathrm{f}} \boldsymbol{v}(\boldsymbol{x}, t) \mathrm{d}V + \oint_{S(t)} \rho^{\mathrm{f}} \boldsymbol{v}\boldsymbol{v} \cdot \boldsymbol{n} \mathrm{d}S = - \oint_{S(t)} p\boldsymbol{n} \mathrm{d}S + \oint_{S(t)} \eta^{\mathrm{f}}(J_2)\, \nabla \boldsymbol{v} \cdot \boldsymbol{n} \mathrm{d}S + \oint_{V} \nabla^{\mathrm{T}} \boldsymbol{v} \cdot \nabla \eta^{\mathrm{f}}(J_2) \mathrm{d}V \tag{14}$$

2.4 Numerical Methods

Geometries and Spatial Discretization

The patient-specific aneurysms geometries were extracted from digital subtraction angiographic (DSA) 3D images, using the open-source package VMTK®, which was used to extract the geometry corresponding to the flow domain. Figure 3 shows the sequence of steps performed in VMTK® to generate the final surface for one of the aneurysms cases studied here: first, the whole surface of the vessels tree is extracted as a computational surface, which is then segmented to obtain only the region where the aneurysm is located and, finally, extracting the aneurysm and surrounding vessels surface which can be send to the process of spatial discretization needed for the numerical discretization technique used to solve the governing equations.

The spatial discretized domain is a computational mesh generated automatically with the `snappyHexMesh` utility of the CFD software used to solve the governing equations, `foam-extend`, version 4.0. This utility generates the so-called *hexa-dominant meshes*, because it creates generic polyhedral cells with a dominant number of hexahedral types of cells in the interior of the domain. The generated mesh also contains a refined layer of prismatic volumes adjacent to the geometry physical wall to increase the spatial resolution, needed to capture the dynamic details of the flow boundary layer.

The aneurysm geometries studied in this text are depicted in Fig. 4 with an indication of their position in the brain arteries tree – with the same model tree shown in Fig. 1b – and Table 1 provides the geometric characteristics of each aneurysm, such as height h_d, neck diameter d_n, parent artery, aspect ratio and mean blood flow rate in the parent artery. We chose aneurysms cases in the main location of their occurrence, contemplating several aneurysm anatomies regarding their size and presence or not of lobular and bleb structures.

Equations Discretization

To solve the system of equations governing the flow problem – Eqs. (1) and (2) with the rheological models, Eq. (10) with Eqs. (3) and (4) – under the boundary conditions presented in Section 2.1, we chose the Finite Volume Method (FVM) (Patankar, 1980; Moukalled *et al.*, 2016), since it is one of the most used numerical methods for CFD applications, through the implementation of the open-source package `foam-extend` (OpenFOAM-Extend, 2017), version 4.0.

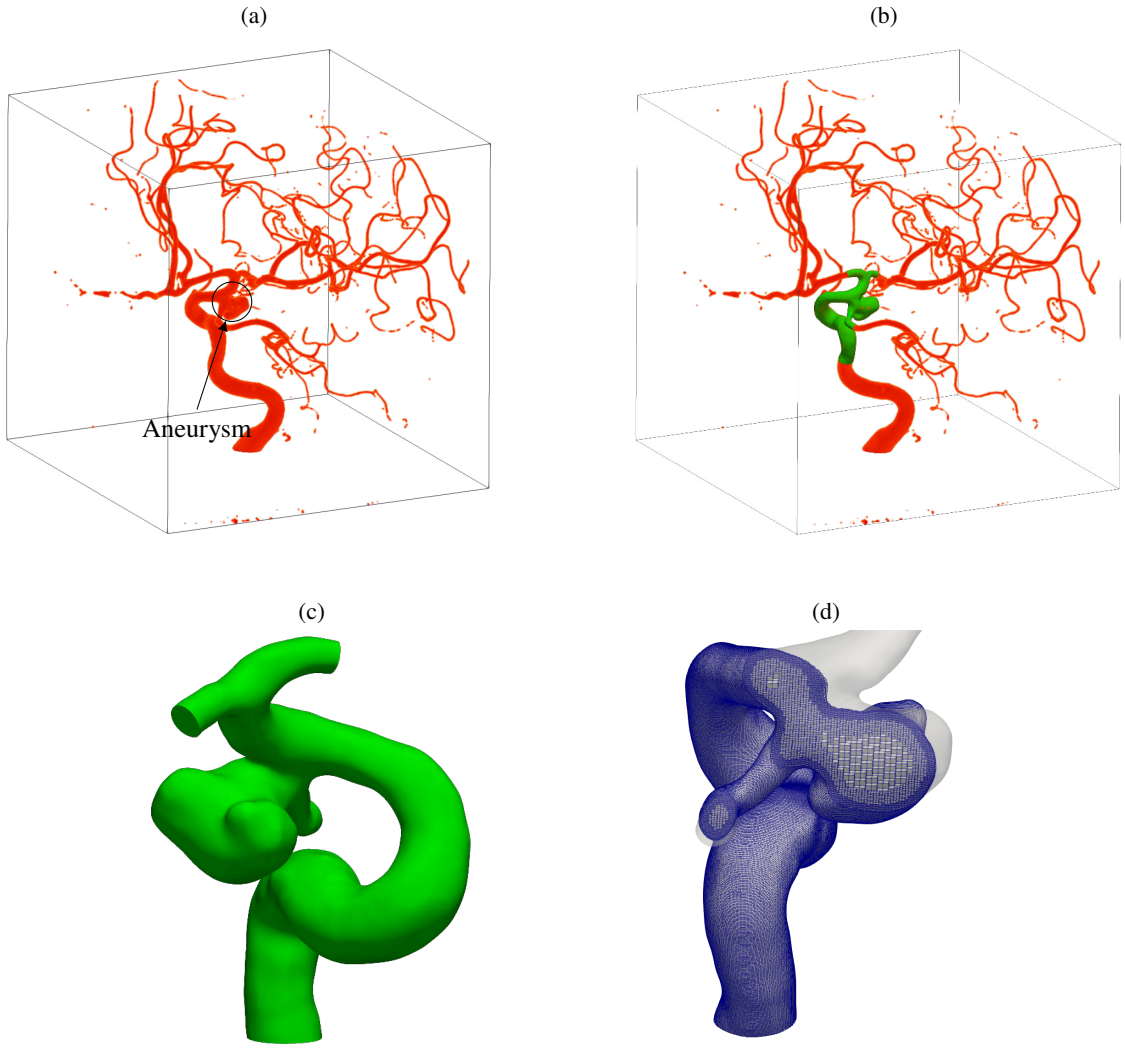

Figure 3. (a) Volume rendering representation of the DSA image of an aneurysm and surrounding vessels (rendered in ParaView®); (b) Segmented surface using VMTK® (as a green surface); (c) final extracted portion of the surface containing the aneurysm geometry and (d) final computational mesh created using the utility `snappyHexMesh` of `foam-extend`, that generates a so-called *hexa-dominant mesh* because most of its control volumes are hexahedra.

Table 1. Geometric parameters of the aneurysm studied here: parent artery and its diameter d_a, neck diameter d_n, dome height h_d and diameter d_d, aspect ratio A_r, the mean blood flow rate through its parent artery, $\bar{q}_a$.

	Parent Artery	d_n (mm)	h_d (mm)	d_d (mm)	d_a (mm)	A_r (-)	$\bar{q}_a$ (ml/s)
Case 1	Right and Left ACA	6.1	4.3	5.0	1.8	0.7	2.5
Case 2	ICA	4.6	6.3	8.8	4.6	1.4	4.3
Case 3	MCA	6.5	18.5	14.1	2.4	2.8	2.5

The `foam-extend` package uses the FVM with collocated variables arranged in a cell-centered discretization of the governing equations. A finite-volume mesh is composed of non-overlapping polyhedral cells with polygonal flat faces and each internal face is shared by two cells; external faces, which compose the boundaries of the domain, belong to only one cell. The complete discretization process of the FVM can be found in more specific literature such as Moukalled *et al.* (2016) and Versteeg and Malalasekera (2007). The pressure-velocity coupling was solved using the Pressure Implicit with Splitting Operators (PISO) algorithm (Issa, 1986). When the FVM is used to discretize a Partial Differential Equations (PDE) on a computational mesh, it generates a linearized system of algebraic equations that can be solved with any iterative

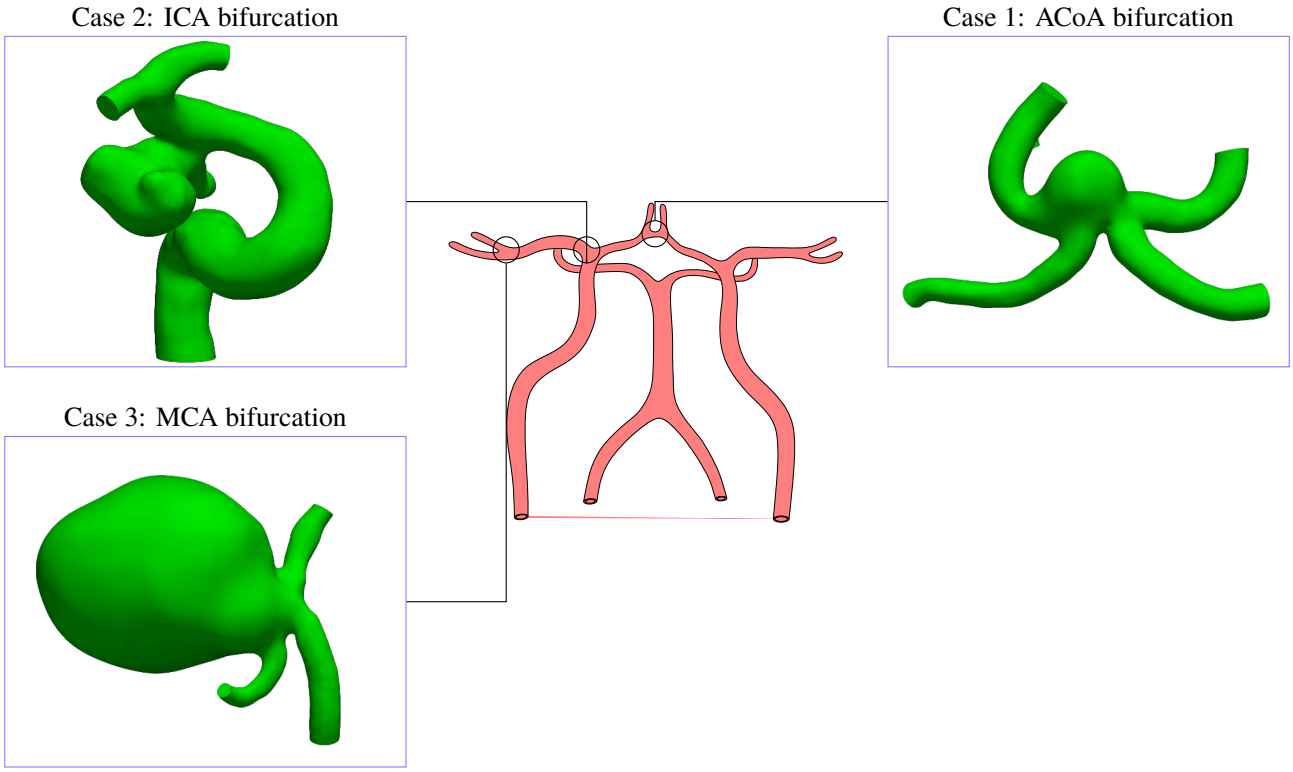

Figure 4. Aneurysm geometries used: case 1 occurring at the Anterior Communicating Artery (ACoA); case 2, an aneurysm occurring on the ICA bifurcation and case 3, a giant aneurysm occurring on the bifurcation of the MCA.

solvers. For example, the system composed of Eqs. (1) and (14) are transformed into the following systems with the FVM:

$$\mathbf{A}^{v}\mathbf{v} = \mathbf{b}^{v} \tag{15}$$

$$\mathbf{A}^{p}\mathbf{p} = \mathbf{b}^{p} \tag{16}$$

respectively, being the pressure system originated from the continutiy equation.

The library `foam-extend` is implemented based on the *object-oriented programming paradigm* (Stroustrup, 2013), using C++ classes. This implementation defines two main *namespaces* called `fvm` and `fvc`: each of them assembles *discretizations* and *calculus* operations, respectively, i.e. `fvm` generates the coefficients of the algebraic system to be solved whereas `fvc` explicitly calculates the calculus operands with field values of the variables being studied. For example, in the language of `foam-extend`, the continuum equation, Eq. (14), is discretized and turned into a system of algebraic equations with the following code:

```
UEqn
   (
          fvm::ddt(U)
          fvm::div(phi, U)
        - fvm::laplacian(fluid.nu(), U)
        - fvc::grad(U) & fvc::grad(fluid.nu())
       ==  -fvc::grad(p)
  );
```

The terms in front of the `fvm` operator yield computational matrices that are assembled in one matrix of coefficients – $\mathbf{A}^{v}$ in Eq. (15) –, while the terms with `fvc` contributes to the vector source of the final linear system.

2.5 Data Analysis

Once completed the simulations, we evaluated the following quantities using ParaView®, an open-source software for post-processing of CFD simulations. This software has a large number of filters that allow processing and displaying all field variables of the flow and wall-fluid interface:

- Velocity field to determine where the flow impinges the aneurysm;
- WSS at the surface wall: the WSS is the magnitude of the traction due to the viscous part of the Cauchy stress tensor, $\boldsymbol{t} = \boldsymbol{n} \cdot \boldsymbol{\tau}$, of the flow on the wall discounted by the normal component of this vector, i.e.:

$$WSS = \|\boldsymbol{WSS}\|_2 = (\|\boldsymbol{t} - (\boldsymbol{t} \cdot \boldsymbol{n})\,\boldsymbol{n}\|)_{\text{wall}} \tag{17}$$

- The strain rate field, defined in 3D flows by Eq. (13):

$$\dot{\gamma} \equiv 2\sqrt{J_2} \tag{18}$$

where J_2 was defined in Section 2.2

We analyze these fields at the peak systole, i.e. for $t \approx 1.1$ s of the cardiac cycle – see Fig. 2a–, where the largest velocity magnitudes occur, therefore the most severe conditions are present next to this instant.

3. RESULTS

One of the requirements in any numerical simulation code is *code verification* (Oberkampf and Trucano, 2002). The code of `foam-extend` is widely used in industrial and academic research and has been tested in several fields. Regarding *validation* of the numerical solution, unfortunately, we were not able to validate the results experimentally; the work of setting up an experimental test for the aneurysm problem is left as a future work. The other requirement is the verification of the numerical accuracy of the simulations presented here. We analyze the numerical accuracy of our results through a mesh-independence analysis.

We evaluated mesh-independence of the numerical solution qualitatively, comparing the spatial distribution of the velocity field on the volume geometry, and quantitatively using the surface area-averaged WSS over the surface of the geometries used. To perform this study, we solved the flow considering the Newtonian fluid model only.

Figure 5 shows the WSS on the surfaces for meshes with ~ 700,000, ~ 1,500,000 and ~ 3,000,000 control volumes for the aneurysm case 2. We see in the figure that there are small qualitative differences regarding the velocity for the three meshes tested, i.e. the overall structure of the velocity field is already established for the mesh with ~ 700,000 control volumes, suggesting that this level of refinement is adequate. Figure 6, on the other hand, shows how the *area-averaged WSS* over the whole mesh surface varies with time, for two cardiac cycles. The area-averaged WSS is defined as:

$$\overline{WSS}_S = \frac{1}{A_S}\left\|\int_S (\boldsymbol{WSS})\,\mathrm{d}S\right\|_2 \tag{19}$$

where S is the wall surface and A_S is its area. The norm of the integral was calculated because WSS is a vector defined on the surface; the figure shows that there are only small differences between the three meshes. Therefore, we conclude that the mesh with ~ 700,000 is sufficiently refined to provided accurate results, at least for the WSS field, which is the main parameter studied here.

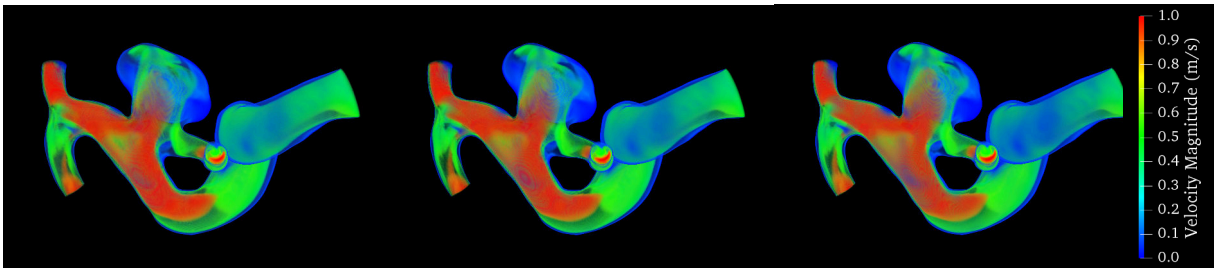

(a) (b) (c)

Figure 5. WSS magnitude distribution at peak systole on the surface of aneurysm of case 2 for computational meshes with (a) ~ 700,000, (b) ~ 1,500,000 and (c) ~ 3,000,000.

For intracranial aneurysms, the literature reports that the risk of rupture is related to areas of small WSS, more specifically, WSS smaller than 1.5 Pa (Shojima *et al.*, 2004). We will consider this value as representing a rupture risk for the aneurysm, although other authors propose that the WSS combined with other hemodynamic parameters are associated with rupture. In the following figures that show the WSS field, we highlight the regions of $WSS < 1.5$ Pa in dark blue to analyze the difference between each model in these regions.

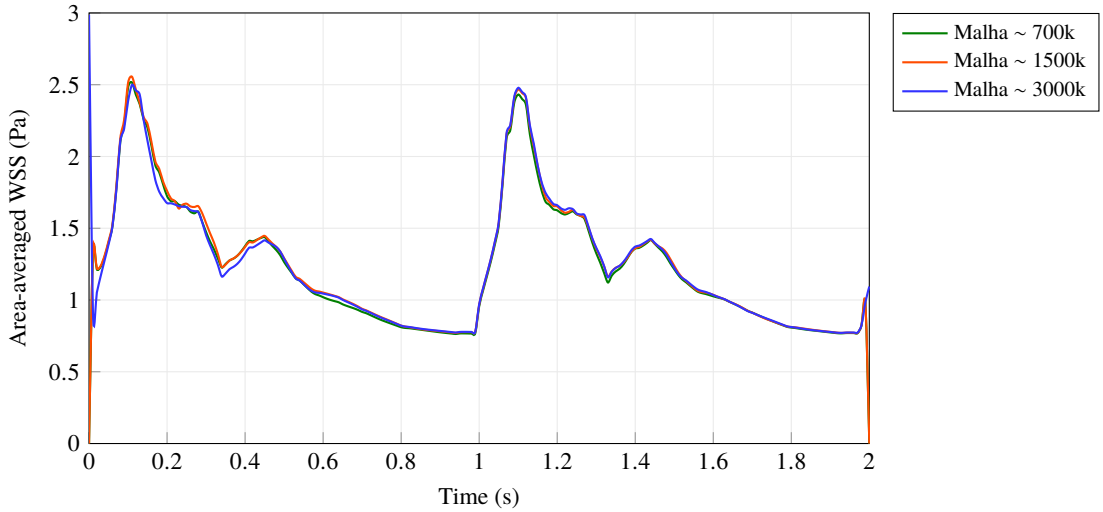

Figure 6. Area-averaged WSS as a function of time for the whole surface for case 2 mesh, with total number of control volumes ~ 700,000, ~ 1,500,000 and ~ 3,000,000 to test mesh independence of the averaged WSS.

We begin by analyzing aneurysm case 1, the smallest case in height. Figure 7 shows the WSS field for it. It is easy to see that there are no evident differences for the WSS field between each fluid model for the view presented in the figure, but this also happens in other regions of the aneurysm. This is an indication that the fluid model have no direct influence on the velocity field for this aneurysm geometry case. Therefore, the Newtonian model could be used to predict the WSS for case 1.

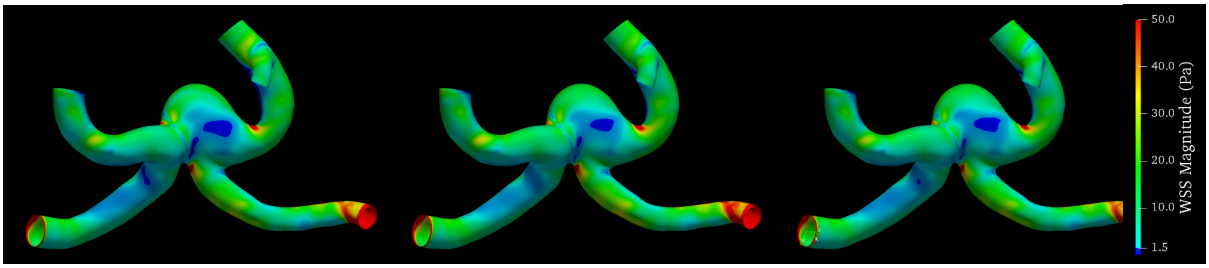

(a) (b) (c)

Figure 7. Comparison of the WSS field for the three fluid models used for case 1: (a) Newtonian model, (b) Casson's model, and (c) Carreau-Yasuda model.

Figure 8 shows a volume rendering view of the velocity field for the three fluid models used at the systole peak. Comparing the results, it is evident that there are no large differences in the overall structure of the field between each model, indicating that the Newtonian model could be used. However, for case 2, in one of its lobular regions which has a dominant recirculating zone, the velocity magnitude increases when the non-Newtonian models are used, as can be noted

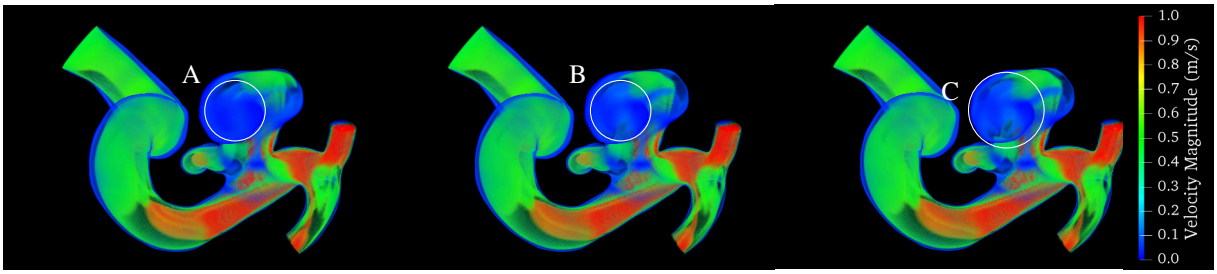

(a) (b) (c)

Figure 8. Comparison of the velocity field at peak systole for the three fluid models used: (a) Newtonian model, (b) Casson's model, and (c) Carreau-Yasuda model.

by comparing the indicated areas A, B and C in Fig. 8.

This trend in the velocity field directly reflects what we see Fig. 9 that shows the WSS field on the domain surface. In this figure, we note that the main differences occur on the aneurysm dome and specifically on the indicated lobular region, whereas on the arteries surface the overall WSS distribution is unchanged. Comparing the areas of low WSS only on the aneurysm surface between the non-Newtonian models with respect to the Newtonian one, there is a decrease of 27.7 % and 33.2 % of these areas when using the Casson and Carreau-Yasuda models, respectively.

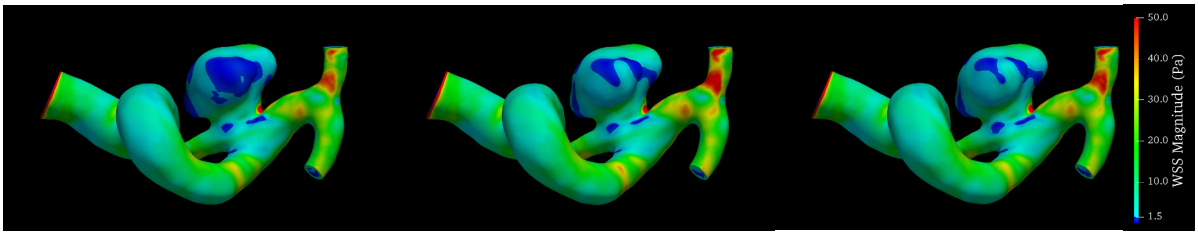

(a) (b) (c)

Figure 9. Comparison of the WSS field for the three fluid models used: (a) Newtonian model, (b) Casson's model, and (c) Carreau-Yasuda model.

Similar to case 2, the case 3, a giant aneurysm, the areas of small WSS are reduced for the non-Newtonian cases, compared with the field for the Newtonian model: note the new large WSS region at the top of the aneurysm dome, marked with label A and B in Fig. 10; the areas of low WSS are reduced of 12.7 % for Casson model and of 13.56 % for Carreau-Yasuda model, compared to the same areas with the Newtonian model.

If we wish, for example, to use CFD results to help the medical practice, by using its results to help physicians to plan a medical procedure, for example, consistent predictions of flow dynamic variables and hemodynamic parameters are very important.

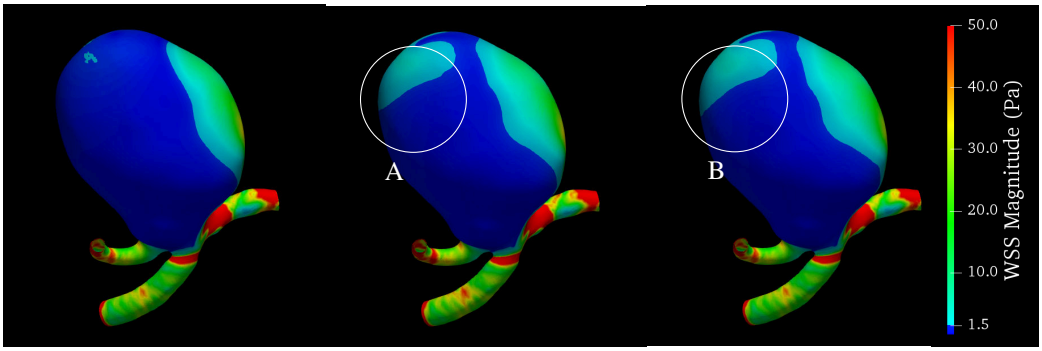

(a) (b) (c)

Figure 10. Comparison of the WSS field for the three fluid models used for case 3: (a) Newtonian model, (b) Casson's model and (c) Carreau-Yasuda model, showing the differences of areas of low WSS.

For both cases 2 and 3, this occurs due to a recirculating flow zone inside the aneurysm dome where the strain rate is smaller than $100\,s^{-1}$ as can be seen in Fig. 11, for case 3, for example – the literature reports (Fung, 1993) that blood flow character is evident below this strain rate level. This type of flow happens in some aneurysms cases depending on the inflow jet direction, for example; for case 2, it happens on the lobular regions on the aneurysm surface and for case 3 due to aneurysm size, therefore, these results suggest that when this type of flow pattern occurs, it may be important to consider a non-Newtonian blood model.

4. CONCLUSIONS

Blood flow in intracranial aneurysms has been the subject of several numerical studies in the past two decades, with the improved physical modeling, including several aspects of this complex problem, such as, for example, the fluid-solid interaction. However, when CFD began to be used to study this biological flow, the Newtonian model was chosen to further simplify the analysis, because accounting for the non-Newtonian character of blood further complicates the problem. Some studies showed that, for arteries that reach the brain, considering blood as a Newtonian fluid is a good hypothesis to correctly predict the WSS *on the vessels walls*, which was also found by our current study, considering the arteries of the patient-specific models used. This can be explained by the level of strain rate found in the flow in

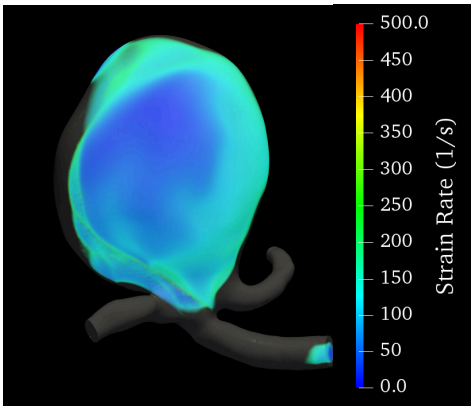

Figure 11. Volume rendering view of the strain rate field of aneurysm case 3, showing a large region on the aneurysm dome with strain rate smaller than 200 s^{-1} – we made the regions with strain rate higher than that value translucent to ease the visualization.

these arteries, which is considerably higher than the level agreed by the literature when blood's behavior departs from the Newtonian behavior. Since aneurysms represent a change in the geometry of the vessels, some cases of aneurysms which present a recirculating flow pattern inside the aneurysm dome are prone to develop low levels of strain rate, revealing the non-Newtonian behavior of blood, as was demonstrated by our simulation of cases 2 and 3.

Therefore, we recommend caution when modeling blood as a Newtonian fluid for any case of intracranial aneurysm. As shown in the results, the WSS was higher when considering Casson and Carreau-Yasuda models compared to the values predicted by the Newtonian model. We leave as future work to simulate more cases that exhibit this flow pattern to further verify our main results.

This kind of study is important when we begin to think in using numerical simulations of flow in intracranial aneurysms to help the medical practice. To this end, correct models should be used to predict the hemodynamic parameters that can help physicians to plan their surgical procedures.

5. ACKNOWLEDGEMENTS

This research was partly supported by resources supplied by the Center for Scientific Computing (NCC/GridUNESP) of the São Paulo State University (UNESP) and Acenet (Dalhousie University).

6. REFERENCES

Bazilevs, Y., Hsu, M.C., Zhang, Y., Wang, W., Kvamsdal, T., Hentschel, S. and Isaksen, J.G., 2010. "Computational vascular fluid-structure interaction: Methodology and application to cerebral aneurysms". *Biomechanics and Modeling in Mechanobiology*, Vol. 9, No. 4, pp. 481–498. ISSN 16177959. doi:10.1007/s10237-010-0189-7.

Bernsdorf, J. and Wang, D., 2009. "Non-Newtonian blood flow simulation in cerebral aneurysms". *Computers and Mathematics with Applications*, Vol. 58, No. 5, pp. 1024–1029. ISSN 08981221. doi:10.1016/j.camwa.2009.02.019.

Cebral, J.R.J.R., Hernández, M., Frangi, A.A.F., Cerrolaza, M., Hernández, M. and Frangi, A.A.F., 2003. "Computational analysis of blood flow dynamics in cerebral aneurysms from CTA and 3D rotational angiography image data". *International Congress on Computational Bioengineering*, Vol. 1, pp. 191–198. URL `http://www.tecn.upf.es/ afrangi/articles/iccb2003.pdf`.

Cokelet, G.R., Merrill, E.W., Gilliland, E.R., Shin, H. and Britten, A., 1963. "The rheology of human blood—measurement near and at zero shear rate". *Journal of Rheology*, Vol. 7, No. 1, p. 303. ISSN 01486055. doi:10.1122/1.548959. URL `http://link.aip.org/link/?JOR/7/303/1&Agg=doi`.

Ford, M.D., Alperin, N., Lee, S.H., Holdsworth, D.W. and Steinman, D.A., 2005. "Characterization of normal cerebrovascular volumetric flow rate dynamics by PC-MRI". *The International Society for Magnetic Resonance in Medicine 13th Annual Meeting*, Vol. 13, p. 1741.

Fukazawa, K., Ishida, F., Umeda, Y., Miura, Y., Shimosaka, S., Matsushima, S., Taki, W., Suzuki, H., Bligh, M. and Others, 2015. "Using computational fluid dynamics analysis to characterize local hemodynamic features of middle cerebral artery aneurysm rupture points". *World Neurosurgery*, Vol. 83, No. 1, pp. 80–86. ISSN 18788769. doi: 10.1016/j.wneu.2013.02.012. URL `http://dx.doi.org/10.1016/j.wneu.2013.02.012`.

Fung, Y.C., 1993. *Biomechanics: Motion, Flow, Stress, and Growth*. Springer. ISBN 0387971246. doi:10.1115/1.2900838.

Hop, J.W., Rinkel, G.J.E., Algra, A. and van Gijn, J., 1997. "Case-Fatality Rates and Functional Outcome After Subarachnoid Hemorrhage". *Stroke*, Vol. 28, No. 3, pp. 660 LP – 664. URL

http://stroke.ahajournals.org/content/28/3/660.abstract.

Isaksen, J.G., Bazilevs, Y., Kvamsdal, T., Zhang, Y., Kaspersen, J.H., Waterloo, K., Romner, B. and Ingebrigtsen, T., 2008. "Determination of wall tension in cerebral artery aneurysms by numerical simulation". *Stroke*, Vol. 39, No. 12, pp. 3172–3178. ISSN 00392499. doi:10.1161/STROKEAHA.107.503698.

Issa, R.I., 1986. "Solution of the implicitly discretised fluid flow equations by operator-splitting". *Journal of Computational Physics*, Vol. 62, No. 1, pp. 40–65. ISSN 10902716. doi:10.1016/0021-9991(86)90099-9.

Lee, C.J., Zhang, Y., Takao, H., Murayama, Y. and Qian, Y., 2013. "The influence of elastic upstream artery length on fluid-structure interaction modeling: A comparative study using patient-specific cerebral aneurysm". *Medical Engineering and Physics*, Vol. 35, No. 9, pp. 1377–1384. ISSN 13504533. doi:10.1016/j.medengphy.2013.03.009. URL http://dx.doi.org/10.1016/j.medengphy.2013.03.009.

Lu, G., Huang, L., Zhang, X.L., Wang, S.Z., Hong, Y., Hu, Z. and Geng, D.Y., 2011. "Influence of hemodynamic factors on rupture of intracranial aneurysms: Patient-specific 3D mirror aneurysms model computational fluid dynamics simulation". *American Journal of Neuroradiology*, Vol. 32, No. 7, pp. 1255–1261. ISSN 01956108. doi:10.3174/ajnr.A2461.

Merrill, E.W., Gilliland, E.R., Cokelet, G.R., Shin, H., Britten, A. and Wells, R.E., 1963. "Rheology of human blood, near and at zero flow: Effects of temperature and hematocrit level". *Biophysics Journal*, Vol. 3, No. 3, pp. 199–213.

Moukalled, F., Mangani, L. and Darwish, M., 2016. *The Finite Volume Method in Computational Fluid Dynamics*, Vol. 113. Springer. ISBN 978-3-319-16873-9. doi:10.1007/978-3-319-16874-6.

Oberkampf, W.L. and Trucano, T.G., 2002. "Verification and validation in computational fluid dynamics". *Progress in Aerospace Sciences*, Vol. 38, No. 3, pp. 209–272. ISSN 03760421. doi:10.1016/S0376-0421(02)00005-2.

OpenFOAM-Extend, 2017. "foam-extend Website". https://sourceforge.net/projects/foam-extend/. [Accessed 19-June-2017].

Patankar, S., 1980. *Numerical heat transfer and fluid flow*. McGraw-Hill Publishing. ISBN 978-0891165224 0. doi:10.1016/j.watres.2009.11.010.

Perktold, K., Resch, M. and Florian, H., 1991. "Pulsatile non-Newtonian flow characteristics in a three-dimensional human carotid bifurcation model." *Journal of Biomechanical Engineering*, Vol. 113, No. 4, pp. 464–75. ISSN 0148-0731. doi:10.1115/1.2895428. URL http://www.ncbi.nlm.nih.gov/pubmed/1762445.

Qureshi, A.I., Janardhan, V., Hanel, R.A. and Lanzino, G., 2007. "Comparison of endovascular and surgical treatments for intracranial aneurysms: an evidence-based review". *Lancet Neurology*, Vol. 6, No. 9, pp. 816–825. ISSN 14744422. doi:10.1016/S1474-4422(07)70217-X.

Robertson, A.M., Sequeira, A. and Owens, R.G., 2009. "Rheological models for blood". In *Cardiovascular Mathematics. Modeling and simulation of the circulatory system*.

Shibeshi, S.S. and Collins, W.E., 2005. "The Rheology of Blood Flow in a Branched Arterial System with Three-Dimensional Model: A Numerical Study". *Applied Rheology*, Vol. 15, No. 6, pp. 398–405. ISSN 1727-7191. doi:10.1017/S1727719100002951.

Shojima, M., Oshima, M., Takagi, K., Torii, R., Hayakawa, M., Katada, K., Morita, A. and Kirino, T., 2004. "Magnitude and Role of Wall Shear Stress on Cerebral Aneurysm. Computational Fluid Dynamic Study of 20 Middle Cerebral Artery Aneurysms". *Stroke*, Vol. 35, No. 11, pp. 2500–2505. ISSN 0039-2499. doi:10.1161/01.STR.0000144648.89172.of. URL http://stroke.ahajournals.org/cgi/doi/10.1161/01.STR.0000144648.89172.of.

Sochi, T., 2013. "Non-Newtonian Rheology in Blood Circulation". pp. 1–26. URL http://arxiv.org/abs/1306.2067.

Steinman, D.A., Milner, J.S., Norley, C.J., Lownie, S.P. and Holdsworth, D.W., 2003. "Image-based computational simulation of flow dynamics in a giant intracranial aneurysm." *AJNR. American journal of neuroradiology*, Vol. 24, No. 4, pp. 559–66. ISSN 0195-6108. doi:10.3174/ajnr.a2121. URL http://www.ajnr.org/content/24/4/559.abstract.

Stroustrup, B., 2013. *The C++ Programming Language*. Addison-Weesley, 4th edition.

The International Study of Unruptured Intracranial Aneurysms Investigators, 2003. "Unruptured intracranial aneurysms: natural history, clinical outcome, and risks of surgical and endovascular treatment". *Lancet*, Vol. 362, pp. 103–110.

Torii, R., Oshima, M., Kobayashi, T., Takagi, K. and Tezduyar, T.E., 2007. "Influence of wall elasticity in patient-specific hemodynamic simulations". *Computers and Fluids*, Vol. 36, No. 1, pp. 160–168. ISSN 00457930. doi:10.1016/j.compfluid.2005.07.014.

Torii, R., Oshima, M., Kobayashi, T., Takagi, K. and Tezduyar, T.E., 2008. "Fluid-structure interaction modeling of a patient-specific cerebral aneurysm: Influence of structural modeling". *Computational Mechanics*, Vol. 43, No. 1, pp. 151–159. ISSN 01787675. doi:10.1007/s00466-008-0325-8.

van Gijn, J., Rinkel, G.J.E., Gijn, J.V. and Rinkel, G.J.E., 2001. "Subarachnoid haemorrhage: diagnosis, causes and management." *Brain : a journal of neurology*, Vol. 124, No. Pt 2, pp. 249–78. ISSN 0006-8950. doi:10.1093/brain/124.2.249. URL http://www.ncbi.nlm.nih.gov/pubmed/11157554.

Van Gijn, J., Kerr, R.S., Rinkel, G.J.E., Gijn, J.V., Kerr, R.S., Rinkel, G.J.E., Van Gijn, J., Kerr, R.S. and Rinkel, G.J.E., 2007. "Subarachnoid haemorrhage." *Lancet*, Vol. 369, No. 9558, pp. 306–318. ISSN 1474-547X. doi:10.1016/S0140-6736(07)60153-6.

Versteeg, H.K. and Malalasekera, W., 2007. *An Introduction to Computational Fluid Dynamics*, Vol. 1. Pearson Prentice

Hall. ISBN 9780131274983.

Wong, G.K.C., Poon, W.S. and Wong, G.K.C., 2011. "Current status of computational fluid dynamics for cerebral aneurysms: The clinician's perspective". *Journal of Clinical Neuroscience*, Vol. 18, pp. 1285–1288. doi: 10.1016/j.jocn.2011.02.014.

Zacharia, B.E., Hickman, Z.L., Grobelny, B.T., DeRosa, P., Kotchetkov, I., Ducruet, A.F. and Connolly, E.S., 2010. "Epidemiology of Aneurysmal Subarachnoid Hemorrhage". *Neurosurgery Clinics of North America*, Vol. 21, pp. 221–233. ISSN 10423680. doi:10.1016/j.nec.2009.10.002.

Zarrinkoob, L., Ambarki, K., Wåhlin, A., Birgander, R., Eklund, A. and Malm, J., 2015. "Blood flow distribution in cerebral arteries". *Journal of Cerebral Blood Flow and Metabolism*, Vol. 35, pp. 648–654. ISSN 15597016. doi:10.1038/jcbfm.2014.241.

7. RESPONSIBILITY NOTICE

The authors are the only responsible for the printed material included in this paper.